*remote sensing*

MDPI

*Article*

# Preliminary Derived DInSAR Coseismic Displacements of the 2022 $M_w$ 5.7 Stolac Earthquake

**Antonio Banko, Fran Mihelin, Tedi Banković and Marko Pavasović ***

Faculty of Geodesy, University of Zagreb, Fra Andrije Kačića Miošića 26, HR-10000 Zagreb, Croatia; antonio.banko@geof.unizg.hr (A.B.); fmihelin@geof.hr (F.M.); tedi.bankovic@geof.unizg.hr (T.B.)
* Correspondence: marko.pavasovic@geof.unizg.hr

**Abstract:** On 22 April 2022, a $M_w$ 5.7 earthquake was generated near Stolac (Bosnia and Herzegovina). The mainshock was succeeded by several aftershocks, three of which were significant. Two $M_b$ 4.3 earthquakes occurred on 23 April 2022, and a $M_w$ 4.8 earthquake was generated on 24 April 2022. Available data from fault mechanism solutions revealed that the mainshock activated a reverse fault, while the aftershock generated a normal fault with a right-lateral component. The Balkan Peninsula stands as one of the most active geodynamic areas in Central and Eastern Europe due to its location within the collision zone between Eurasian and African tectonic plates and the Anatolian microplate. Recorded earthquakes in Bosnia and Herzegovina are related to the energy generated by the subduction of the African tectonic plate under Eurasia. Furthermore, the seismicity of Bosnia and Herzegovina, particularly its southern part, is profoundly influenced by the subduction of the Adriatic microplate under the Dinarides. The Dinarides are a mainly fold and thrust belt that extends from the Southern Alps in the northwest to the Hellenides in the southeast and make dominant the tectonic system of Bosnia and Herzegovina. In this study, two pairs of SAR images obtained from the Sentinel-1 satellite mission were utilized to generate satellite LOS surface displacements using the DInSAR method. Moreover, LOS displacements were decomposed into vertical and east–west horizontal components by combining ascending and descending satellite orbits. Ultimately, the InSAR results were analyzed and compared with the data obtained from the CROPOS CORS GNSS station in Metković (MET3).

**Keywords:** DInSAR; interferogram; coseismic deformation; Stolac $M_w$ 5.7 earthquake; GNSS



**Citation:** Banko, A.; Mihelin, F.; Banković, T.; Pavasović, M. Preliminary Derived DInSAR Coseismic Displacements of the 2022 $M_w$ 5.7 Stolac Earthquake. *Remote Sens.* **2024**, *16*, 1658. https://doi.org/10.3390/rs16101658

Academic Editor: Dusan Gleich

Received: 5 March 2024
Revised: 18 April 2024
Accepted: 6 May 2024
Published: 8 May 2024



## 1. Introduction

On 22 April 2022 (21:07 UTC), a 5.7 $M_w$ earthquake occurred in the southern territory of Bosnia and Herzegovina (BiH) ~15 km southeast of Stolac (Figure 1). After the mainshock, several aftershock earthquakes transpired; two 4.3 $M_b$ were generated on 23 April at 02:20 UTC and 02:34 UTC, respectively, and one 4.8 $M_w$ was generated on 24 April 2022 (04:27 UTC). In the following days after the last aftershock, there were no recordings of additional $M > 2.5$ aftershocks.

A focal mechanism solution from the United States Geological Survey (USGS; https://www.usgs.gov/, accessed on 1 March 2023) and the European–Mediterranean Regional Centroid-Moment Tensors (RCMT; http://rcmt2.bo.ingv.it/, accessed on 10 January 2024) revealed that the main event activated a reverse fault (Table 1, Figure 1). Both the mainshock and succeeding aftershocks can be characterized as shallow earthquakes with a depth of ~10–20 km. The earthquake was felt across BiH and neighboring countries. The Stolac earthquake stands as the most powerful seismic event in the territory of BiH in the 21st century. However, the most devastating earthquake in BiH history remains the 1969 6.1 $M_w$ earthquake that struck Banja Luka.

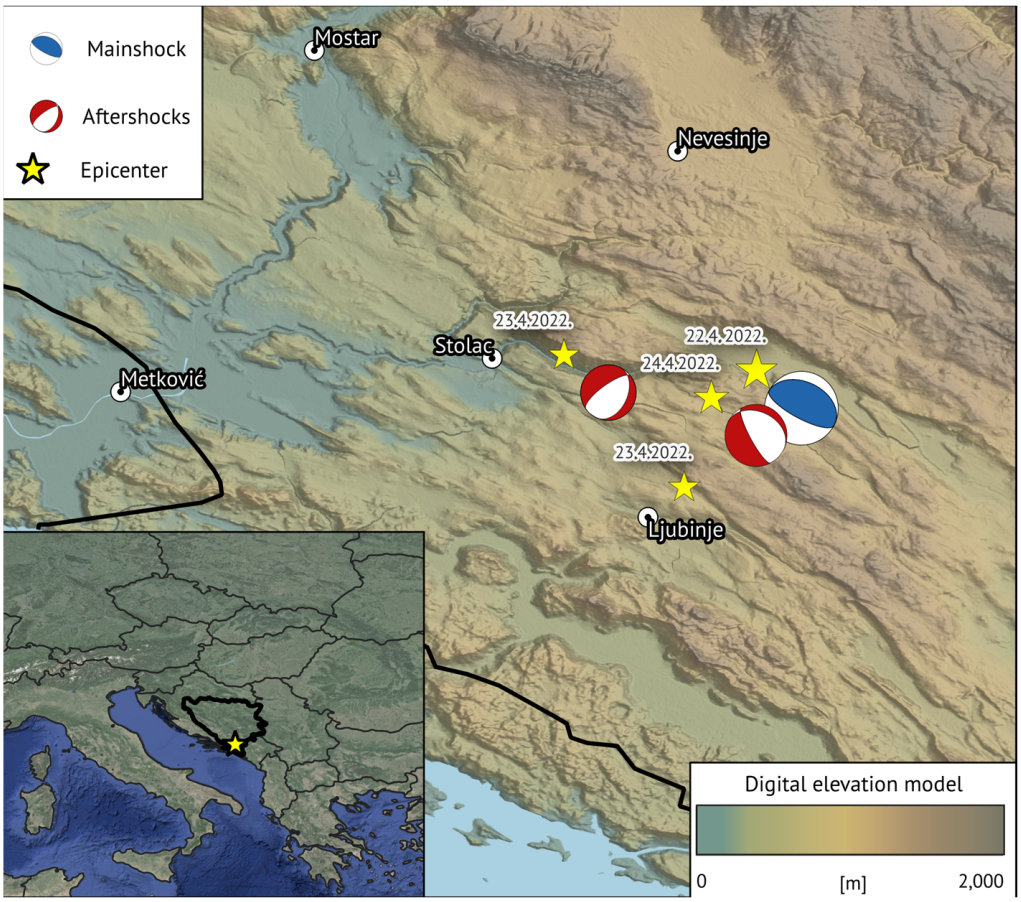


**Figure 1.** Epicenters and lower-hemisphere projections of fault plane solutions for mainshock (comprehensive quadrants are shaded in blue) and aftershocks (comprehensive quadrants are shaded in red), as reported in Table 1.

**Table 1.** The date, time of occurrence, hypocentral coordinates, magnitudes, and Strike, Dip and Rake parameters of the mainshock and succeeding aftershocks. The data for the third aftershock that occurred on 23 April were not available. [1] USGS [1] and RCMT [2].

| No. | Date | Time [UTC] | Lat. Origin [°N] | Lon. Origin [°E] | Magnitude [$M_w$, $M_L$, $M_b$] | Depth [km] | Strike [°] | Dip [°] | Rake [°] | Source [1] |
|---|---|---|---|---|---|---|---|---|---|---|
| 1 | 22 April 2022 | 21:07:48<br>21:07:49 | 43.074<br>43.07 | 18.180<br>18.16 | 5.71 $M_w$<br>5.71 $M_w$ | 10<br>10 | 298<br>295 | 18<br>25 | 94<br>87 | USGS<br>RCMT |
| 2 | 23 April 2022 | 02:20:27<br>02:20:28 | 43.087<br>43.08 | 18.018<br>18 | 4.30 $M_b$<br>4.38 $M_w$ | 10<br>10 | -<br>25 | -<br>28 | -<br>-116 | USGS<br>RCMT |
| 3 | 23 April 2022 | 02:34:22<br>- | 42.976<br>- | 18.119<br>- | 4.30 $M_b$<br>- | 10<br>- | -<br>- | -<br>- | -<br>- | USGS<br>RCMT |
| 4 | 24 April 2022 | 04:27:53<br>04:27:54 | 43.051<br>43.05 | 18.142<br>18.15 | 4.80 $M_w$<br>4.76 $M_w$ | 10<br>19 | 276<br>296 | 16<br>21 | -146<br>-124 | USGS<br>RCMT |

The Balkan Peninsula is one of the most active geodynamical regions in Europe, primarily due to the collision between the African and Eurasian tectonic plate and Anatolian microplate and the subduction of the Adriatic microplate under the Eurasian plate [3,4]. Additionally, the northward motion of the African plate and sliding beneath the European continent primarily influences the principal horizontal stress directions in the BiH region [5], consequently leading to numerous recorded earthquakes in this region [6]. Furthermore, GNSS campaigns have revealed the northward motion and convergence of the Dinarides with the Southern Alps [7]. Earthquakes in the BiH region are mostly concentrated in the southwestern part of the BiH (Figures 2–7) which lays within Outer Dinarides with the most powerful events occurring along the Sarajevo fault [5]. The Dinarides, i.e., Dinaric Alps,

are the dominant and relatively young tectonic system in BiH, oriented in the northwest–southeast direction. This system extends from the Southern Alps in the northwest to the Hellenides in the southeast, constituting a significant geotectonic component of the Southern Alps [5,8,9]. In the Mediterranean region, various types of faults are present. The Apennine Peninsula is distinguished by the prevalence of normal faults, whereas the Adriatic coast and the Dinarides exhibit the presence of reverse faults [10].

The Balkan region, including Bosnia and Herzegovina, is composed of several mobile belts that originated during the formation of the Alpine–Himalayan belt [3]. BiH lies in the central part of the Dinarides, and the presence of active seismotectonic zones in the region is a result of the movement of segments within the Adriatic microplate. Seismogenic active zones, varying in size, the extent of movement and the resistance of the Dinarides' mass are illustrated in Figure 2. These zones are closely related to faults on the Earth's surface, each identified and characterized by one or more dominant tectonic structures [11]. Stolac is located within the Dinaric carbonate platform geotectonic zone which is part of the Livno–Tihaljina seismogenic active zone (Figure 2).

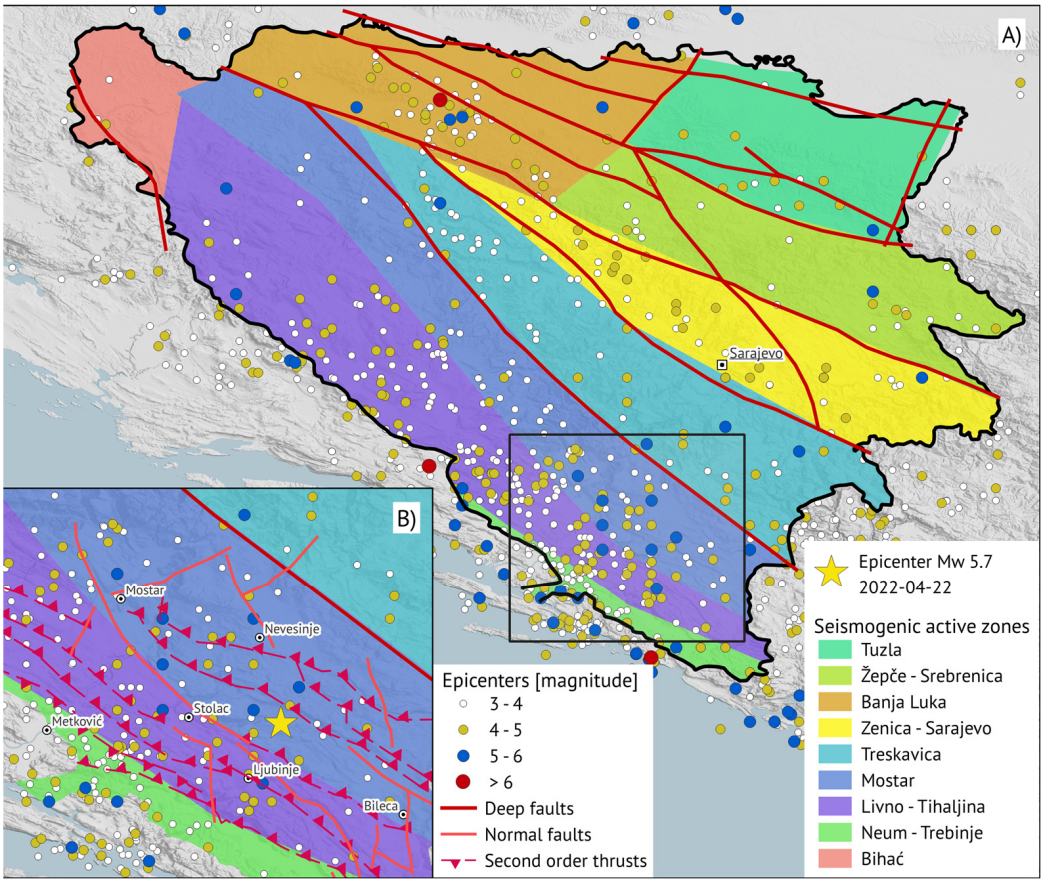


**Figure 2.** (**A**) shows seismogenic active zones and deep faults on the territory of BiH (modified after [11,12]). (**B**) shows deep faults, normal faults and second-order thrust fault structures of the region of interest [11–13]. Earthquake epicenters of the 2020 update of the European Seismic Hazard Model (ESHM20) [14–16] limited to an area between 42.3° and 45.6°N and 15.5° and 20°E and with magnitude > 3.5 are displayed here.

Geodetic data, obtained by ground- or space-based (satellite-based) techniques, can be used to determine the slip motion that occurred during an earthquake. A satellite-based technique can capture coseismic displacements with the use of satellite images, collected at regular intervals, without prior knowledge of the earthquake's location. A ground-based technique in contrary requests a surveyed network to be in place before the earthquake [17]. By taking advantage of the satellite-based technique's huge potential, the Differential Interferometric Synthetic Aperture Radar (DInSAR) method was developed. DInSAR is an active satellite-based remote sensing technique that can be used to quantify very small surface displacements in continuous, large areas and has advantages of high accuracy, high resolution, all-weather adaptability, low cost and inaccessible area coverage [18]. The technique exploits the very high stability of the satellite orbits to determine information about the phase difference between two or more SAR images looking at the same scene from comparable geometries [19,20]. In this research, coseismic ground displacements of the 2022 5.7 $M_w$ Stolac earthquake were determined using the DInSAR technique on Sentinel-1 radar images. Two pairs of C-band Sentinel-1 images acquired from an ascending and descending orbit were used to generate surface motion. As both ascending and descending orbits were used, it was possible to derive 3D surface motion from satellite line-of-sight (LOS) surface displacements.

The quality and reliability of derived DInSAR data were compared with the data obtained from the CROPOS (Croatian Positioning System) GNSS CORS (Continuously Operating Reference Station) Metković (MET3) and processed with Precise Point Positioning (PPP) static and kinematic solutions.

## 2. Previous Research

According to lithofacial development, more than half of the BiH territory dates from the Mesozoic period and is composed of different sedimentary, metamorphic and igneous rocks, while the rest of the territory dates from the Cenozoic period and Paleozoic period. The Cenozoic period is composed of marine, lake, river and volcanic sediments, whilst the earliest Paleozoic period is composed of different stone masses developed from the Silurian to Triassic age [21,22]. The majority of BiH encompasses the Dinarides, situated between the Adriatic Sea to the southwest and the Pannonian basin to the northeast [21]. The Dinarides are a diverse geological unit organized into Outer or External and Inner Dinarides [23] (Figure 3). This intricate assemblage reflects a nuanced interplay of geological processes, shaping the region's complex and dynamic geological history. The Outer Dinarides (Figure 3) are an active fold and thrust belt which prevail on coastal and offshore areas and extend from western Slovenia to Montenegro. They have formed since Jurassic times by progressive compression towards the west between the eastern edge of the Adriatic microplate and the inner Dinaric block [8,24,25].

From Figure 3, it can be observed that different types of faults can be distinguished in the Mediterranean. While the Apennine Peninsula is characterized by the existence of normal faults, the Adriatic coast and the Dinarides are characterized by thrust faults. Prevailing horizontal movements of the Dinarides and the Adriatic are shown in the work of Anderson and Jackson [26], Marjanović [27], Pavasović [28] and Pavasović et al. [29]. From there, it is evident that movements of the Adriatic microplate towards the NNE increases the tectonic activity in the Adriatic regional structure unit and in the contact area with the Dinarides.

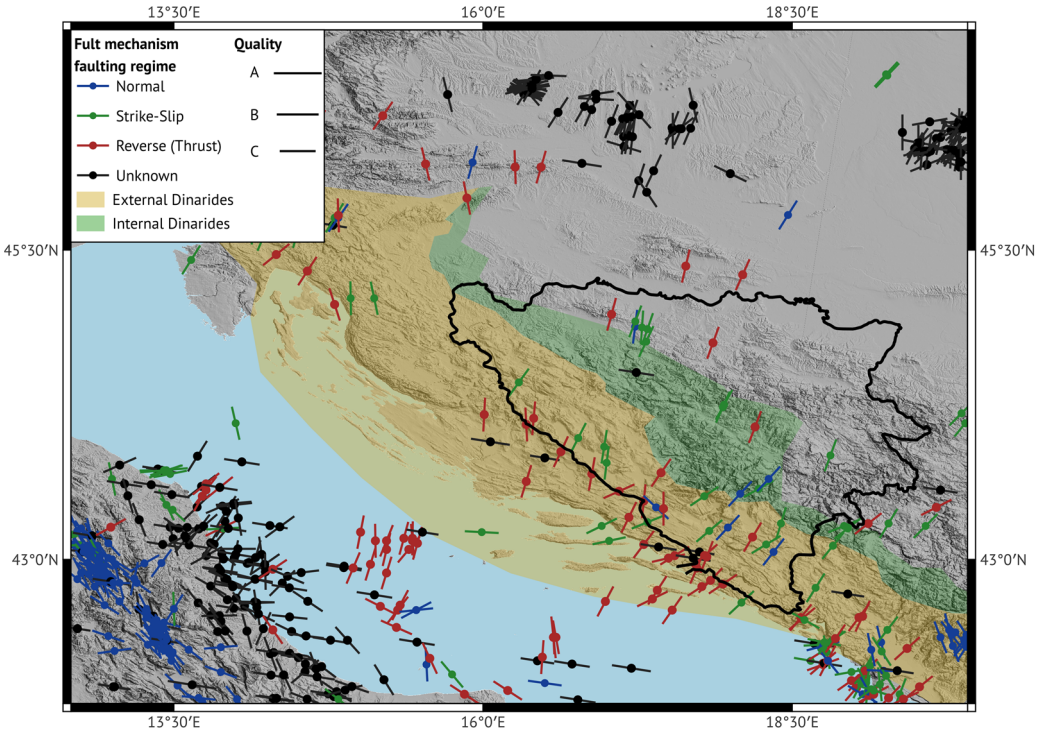


**Figure 3.** A stress map for the Adria region from the upper 40 km of the crust. It displays the orientation of the horizontal stress. The length of the stress symbol denotes the data quality, with A as the best quality (±15°), B data with good quality are within ±20° and C denotes the lowest reliable quality and is within ±25° (modified after [30]). The shaded area represents the External and Internal Dinarides (simplified after [31] (with references therein) and [32]).

The Alpine–Dinarides region characterizes significant crustal thickness variations ranging from 20 to 50 km [33–36]. The Adriatic Sea is underlain by a continental crust with a thickness ranging from 35 to 40 km. It is bordered to the west and east by the flexural foredeep basins of the Apennines and Dinarides, as noted in [37]. Figure 2 shows deep faults and main seismogenic zones in BiH, and as is shown in Omerbashich and Sijarić [5], the longest deep fault of BiH is the Sarajevo fault exceeding 300 km in length and reaching Moho at a depth of 35 km to 40 km. All main transverse deep faults submerge under the Sarajevo fault, and high seismicity along transverse deep faults and low seismicity along the longest Sarajevo fault indicate that an M 6 earthquake or stronger can occur near the Sarajevo fault and transverse deep faults [5].

The first seismograph on the BiH territory was installed in Sarajevo in 1904, and since then, the strongest earthquake recorded on an instrument occurred in 1923 in the southern part of BiH near Tihaljina with a moment magnitude of 6.1. The Tihaljina earthquake took place in the locality of the Livno and Mostar fault. The most devastating earthquake in BiH occurred in 1969 in Banja Luka with a 6.1 $M_w$ (6.5 $M_L$) with a 25 km focal depth and intensity between the VII° and IX° on the Mercalli–Cancani–Sieberg scale (MCS) [38]. In 1962, a 5.9 $M_w$ earthquake hit Mount Treskavica with a focal depth of 15 km.

Crucial data for conducting a hazard assessment are the historical earthquake records specific to the region of interest, embodied within an earthquake catalogue. The Global Seismic Hazard Assessment Program (GSHAP) was conducted in 1992–1998 to promote prevention and mitigate the risks of natural disasters [39,40]. In the GSHAP framework, the Adriatic region serves as a link between continental Europe and the Mediterranean. Under the GSHAP, the earthquake catalogue comprised two primary components: the Italian catalogue and the catalogue encompassing Adriatic Balkan countries, including Slovenia, Croatia, Montenegro (formerly Yugoslavia), Albania and Greece. Slejko et al. [41],

with references therein, detailed fault plane solutions for significant earthquakes in the Adria region.

The Harmonization of Seismic Hazard Maps for the Western Balkan Countries Project (BSHAP) funded by NATO Science for Peace and Security Program was active from 2007 to 2014 with the main objective of preparing new seismic hazard maps for the Western Balkan region [3,42,43]. BSHAP, a unified and harmonized earthquake catalogue, covers the geographic area between 38.0° and 47.5°N and 12.5° and 24.5°E and includes 26,118 earthquakes that occurred in the West Balkan region between 510BC and 2012 [42]. The spatial distribution of the earthquakes in the BSHAP catalogue is shown in Figure 4 where all the contributing countries are shaded. The map shows earthquakes with M $\geq$ 3.5 in the period from 510BC to 1969 and earthquakes with M $\geq$ 3.0 in the period from 1970 to 2012. The initial BSHAP catalogue was updated with earthquakes with an M between 3.0 and 3.5 that happened between 1970 and 2012 [42].

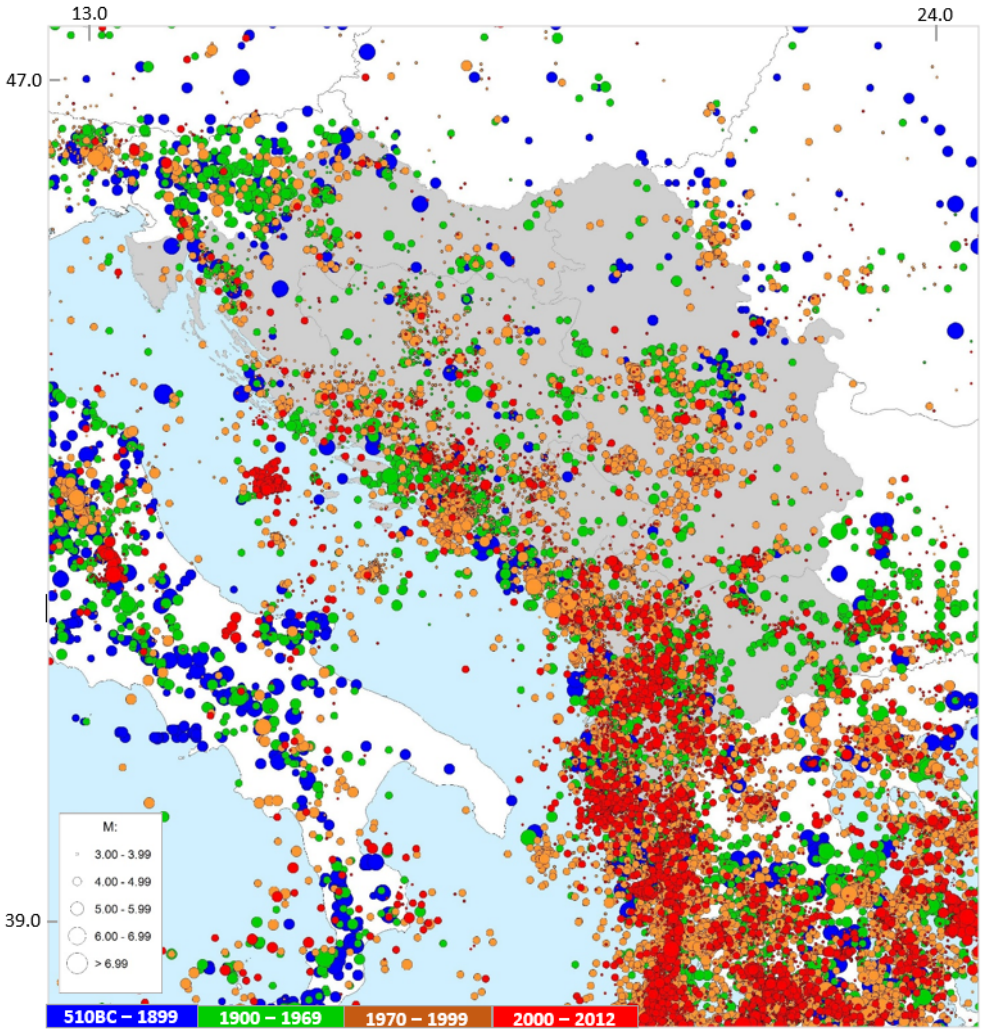


**Figure 4.** An earthquake's location from the BSHAP catalogue with M $\geq$ 3.5 in the period from 510BC to 1969 and earthquakes with M $\geq$ 3.0 in the period from 1970 to 2012. The countries that contributed to the BSHAP catalogue are shaded. The image is adapted with permission from Markusic et al. [42].

Earthquakes obtained from USGS [1], RCMT [2] and ISC-GEM [44] for the period between 1906 and 2021 and with magnitude $\geq$ 2.5 are shown in Figure 5. Most earthquakes had a magnitude in the range 2.5–3.5, i.e., which makes up around 65% of earthquakes, while large-scale earthquakes (magnitude above 6) make up ~1% of all earthquakes.

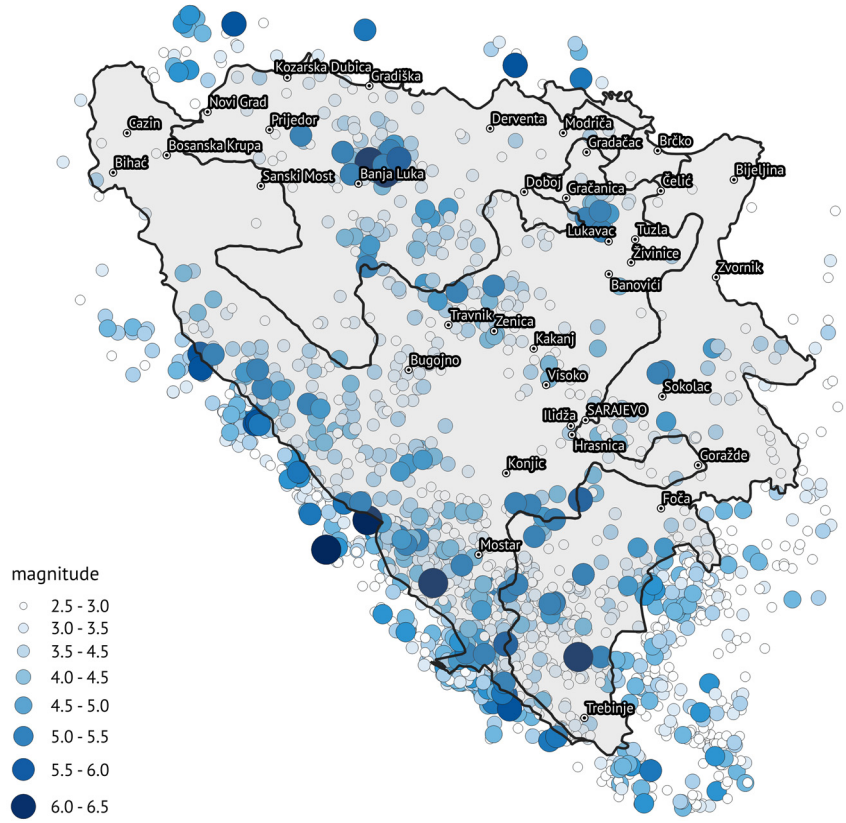


**Figure 5.** A map of earthquake epicenters in the territory of Bosnia and Herzegovina (M $\geq$ 2.5) from 1906 until 2021. Data were obtained from USGS [1], RCMT [2] and ISC-GEM [44].

Data from previous precise leveling campaigns (1931 vs. 1873 and 1961 vs. 1946) were used to determine crustal uplift in the region and are in agreement with the general tectonic tendency in the region [5]. Geodynamic research using GPS techniques in BiH started in 1998 [21] and provides an insight into crustal uplift where the horizontal movement of faults in the northwest direction was observed [5]. Due to an insufficient density of GPS stations, geodynamical studies that used GPS were inadequate to determine horizontal displacements such as the compression and expansion of the lithosphere, but the current coverage of BiH with GPS campaigns is satisfactory, as well as the sufficient density of stations in the network, which enables further geodynamic research [5].

It is evident from the data of the Federal Hydrometeorological Institute of BiH [45] that the Mostar basin area represents a long-term moderately active seismic area. During the period from 2001 to 2020, the Dinarides chain, and particularly the Metković–Mostar–Stolac area, represents a belt of increased seismic activity. In comparison with the rest of the region (interior of BiH, Adriatic coast), the area of study has the largest accumulation of earthquakes, as it is shown in Figure 6. From Figure 5, it can be concluded that the Metković–Mostar–Stolac area is a belt of increased seismic activity, and it can be seen that these data are in accordance with the data obtained from Bijedić [45].

In preceding chapters, it has been elucidated that various geological formations and fault systems traverse the territory of Bosnia and Herzegovina (BiH) and consequently, the observed area, and while the primary focus of this research revolves around geodetic observations and the quantitative analysis of derived outcomes, some insights into how InSAR can help to better understand regional geological features and fault systems have also been discerned and are described upon in subsequent sections of this paper.

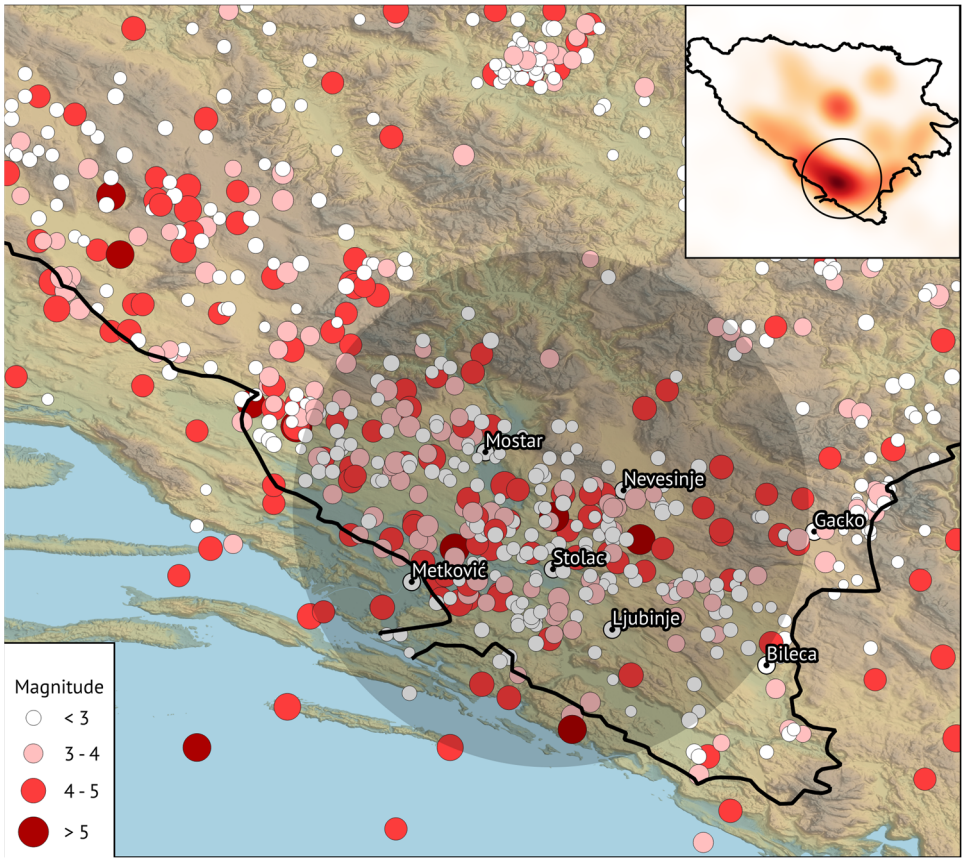


**Figure 6.** Seismic activity on the territory of BiH in the period from 2001 to 2020 where it is visible that the Metković–Mostar–Stolac area represents a belt of increased seismic activity (gray circle) (modified after [45]). Earthquake size is depicted by Richter magnitude, also referred to as local magnitude ($M_L$). Richter magnitude utilizes a logarithmic scale and is based on surface wave amplitudes recorded by nearby seismographs [14].

## 3. Study Area and Data

The main objective of this article was to investigate the DInSAR ground surface displacement in the southern part of BiH due to the 2022 earthquake that took place near the city of Stolac. The earthquake took place on 22 April, with the epicenter 15.6 km SSW from Ljubinje (Republic of Srpska, BiH), 29.9 km SE from Bileća (Republic of Srpska, BiH), 42.4 km SSE from Trebinje (Republic of Srpska, BiH), 42.5 km NW from Mostar (Federation of BiH, BiH) and 48.5 km S from Dubrovnik (Croatia) [USGS; https://www.usgs.gov/, accessed on 21 April 2023]. The study field is shown in Figure 7. Also, this study estimated the impact of the earthquake on the larger surrounding city of Metković (Croatia) (Figure 7).

Two pairs of Interferometric Wide (IW) swath Single Look Complex (SLC) radar images from the Sentinel-1A satellite were used in this research (Table 2). VV polarized images were collected from both an ascending and descending orbit with a 12-day revisit cycle. The Sentinel-1A satellite was launched in 2014 and is controlled by the European Space Agency (ESA). Its sensor operates in C-band (5.54 cm wavelength) with four possible acquisition modes (SM, IW, EW and WV). IW mode consists of three sub-swaths with a 250 km wide footprint of the Earth's surface, and IW SLC radar images have a spatial resolution of 5 m × 20 m in range and the azimuth direction [46].

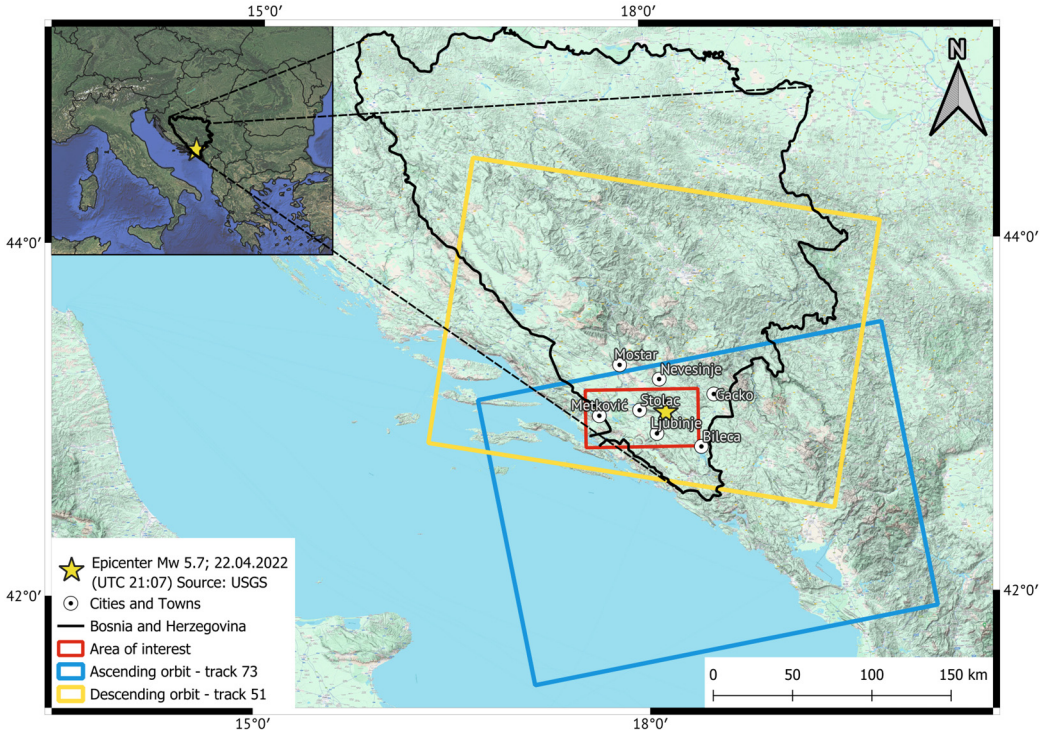


**Figure 7.** The location of the study area and coverage of Sentinel-1 SAR data in the Stolac (BiH) region.

**Table 2.** Interferometric pairs used in the DInSAR processing of the 5.7 $M_w$ 22 April 2022 Stolac earthquake. $B_{perp}$ and $B_{temp}$ represent the perpendicular and temporal baseline used for DInSAR processing, respectively.

| Satellite | Orbit | Track/Frame | Master Image | Slave Image | $B_{perp}$ [m] | $B_{temp}$ [Day] |
|---|---|---|---|---|---|---|
| Sentinel-1A | Ascending | 73/135 | 19 April 2022 | 1 May 2022 | 44.30 | 12 |
| Sentinel-1A | Descending | 51/447 | 18 April 2022 | 30 April 2022 | 2.92 | 12 |

## 4. Results

### *4.1. DInSAR Processing*

Two pairs of SLC Sentinel-1A images were processed with interferometric synthetic aperture radar Scientific Computing Environment (ISCE) software (version 2.6.3) [47] to generate coseismic interferograms of the 2022 Stolac region, BiH, earthquake. A flowchart of DInSAR processing used in this research is depicted in Figure 8. Coregistrations of images were based on precise orbits and a 1 arc sec Shuttle Radar Topography Mission (SRTM) digital elevation model (DEM) [48]. The SRTM DEM was also used to remove flat-earth and topographic phase artifacts from the images and to geocode them. An adaptive power spectrum filter [49] with an alpha value of 0.9 was used to lower phase noise and to improve measurement accuracy and phase unwrapping. A multilook ratio of 12:5 in range and azimuth directions was applied to obtain a ~70 m pixel posting of the geocoded interferograms. The unwrapping of the 2π moduli wrapped interferograms was conducted using the minimum cost flow (MCF) SNAPHU (Statistical-Cost, Network-Flow Algorithm for Phase Unwrapping) algorithm [50]. In post-processing, a Global Atmospheric Correction Online Service (GACOS) [51–53] for InSAR was applied to reduce tropospheric phase delay in the geocoded interferograms.

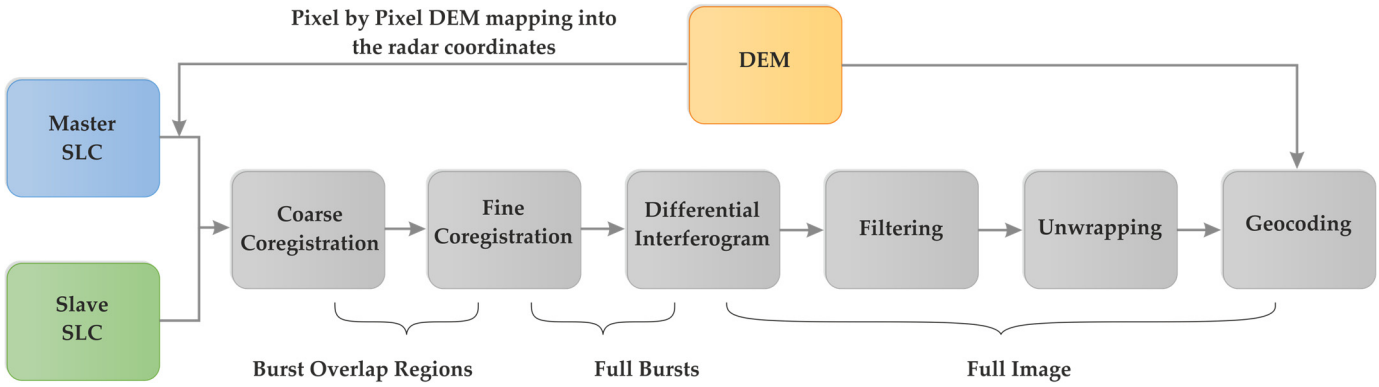


**Figure 8.** Flowchart of DInSAR processing steps using TOPS Sentinel-1 radar images.

Figure 9 shows a wrapped interferogram of ascending orbit, while Figure 10 shows a wrapped interferogram of descending orbit.

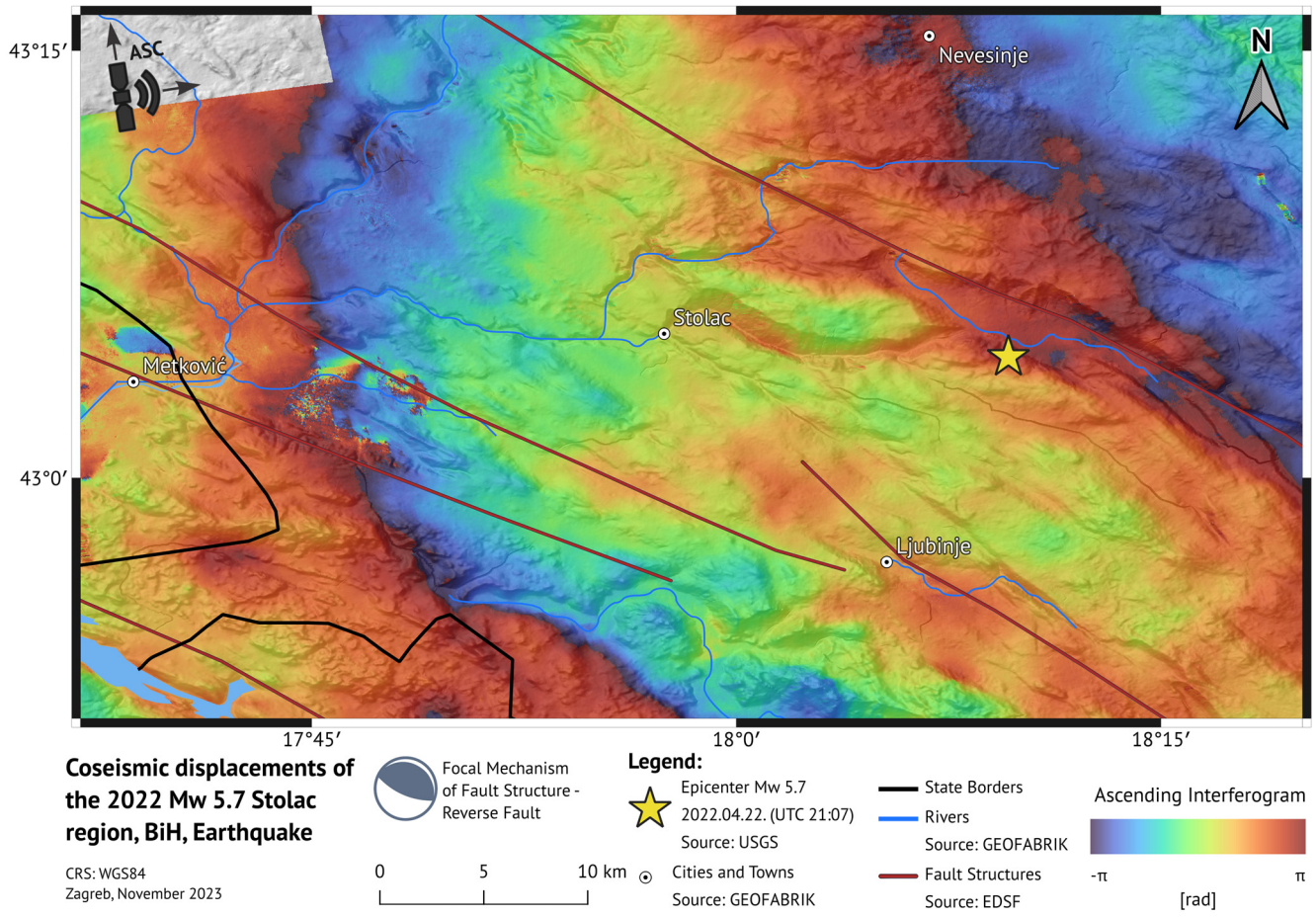


**Figure 9.** Sentinel-1 wrapped interferogram of ascending orbit (track 73) showing ground deformation caused by $M_w$ 5.7 22 April 2022, Stolac earthquake.

From Figure 9, it can be noticed that the phase change of the wrapped interferogram follows the local fault structure. Low coherence and hence unreliable data are possible around the city of Metković, as well as around Lake Svitavsko (between cities of Metković and Stolac).

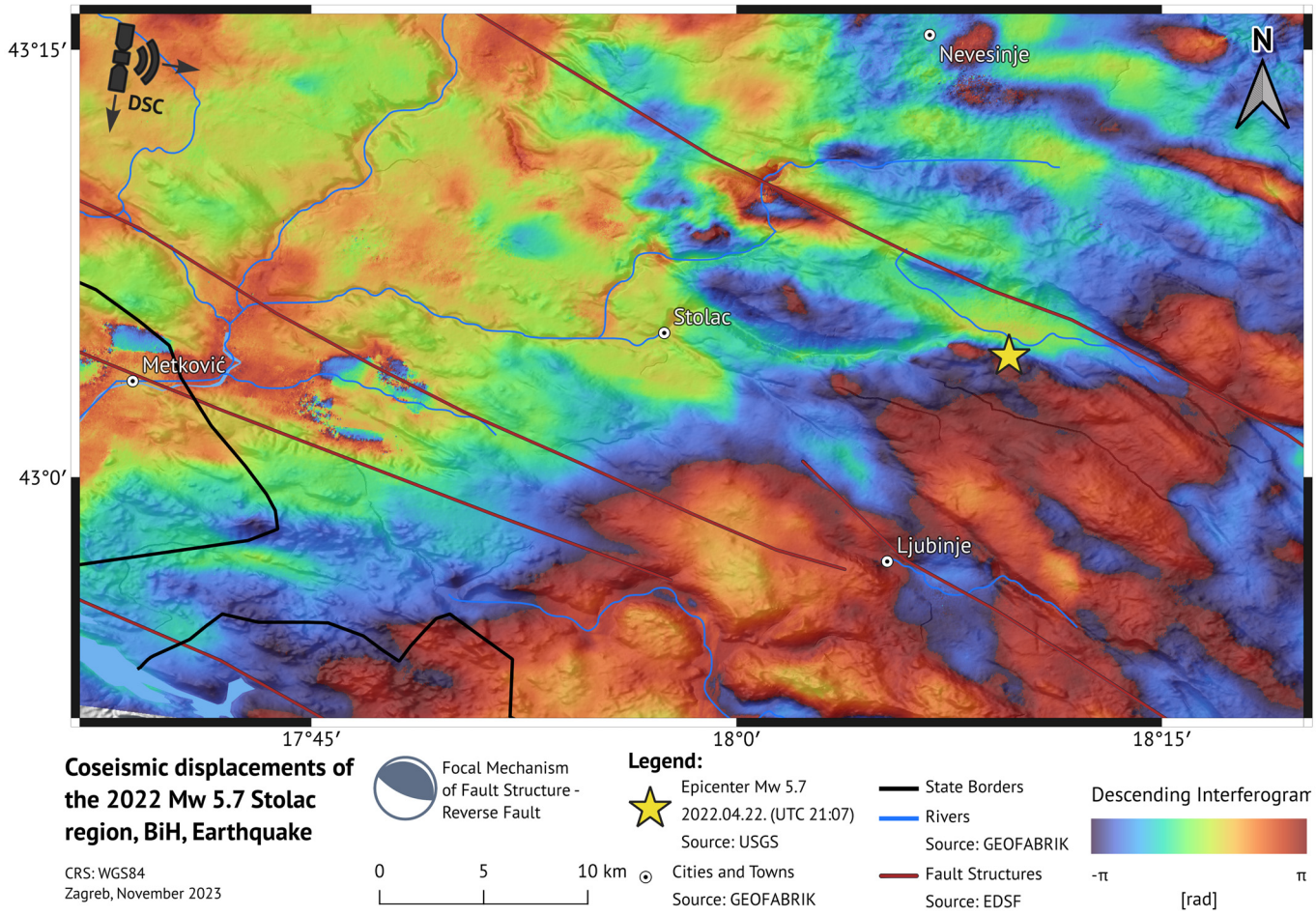


**Figure 10.** Sentinel-1 wrapped interferogram of descending orbit (track 51) showing ground deformation caused by $M_w$ 5.7 22 April 2022, Stolac earthquake.

In order to make the results intuitive, comparable and usable, angular units of unwrapped phase shifts need to be converted into metric units which yield maps of LOS ground displacements. LOS displacements can be positive or negative, meaning it can represent either uplift and motion towards the antenna or subsidence and motion away from the antenna direction.

As the image acquired on the earlier date was used as a master in the InSAR process, negative values (blue color in the maps) of the descending LOS displacements indicate a combination of subsidence and horizontal displacement in the direction away from the sensor. On the other hand, the red color indicates areas with positive values where a combination of uplift and horizontal motion towards the sensor is present.

The LOS displacement map of the ascending orbit has predominant negative values with a minimum of −6 cm. In Figure 11, no positive values means that almost the whole image area is moving away from the sensor. Motion away from the sensor implies movement to the east and includes subsidence along with horizontal eastward motion.

The LOS displacement map of the descending orbit has predominant positive values with a maximum of 5 cm (Figure 12) indicating that image area has a character of uplift and motion towards the satellite. In contrary to ascending orbit, descending displacements are characterized by west horizontal motion and surface uplift.

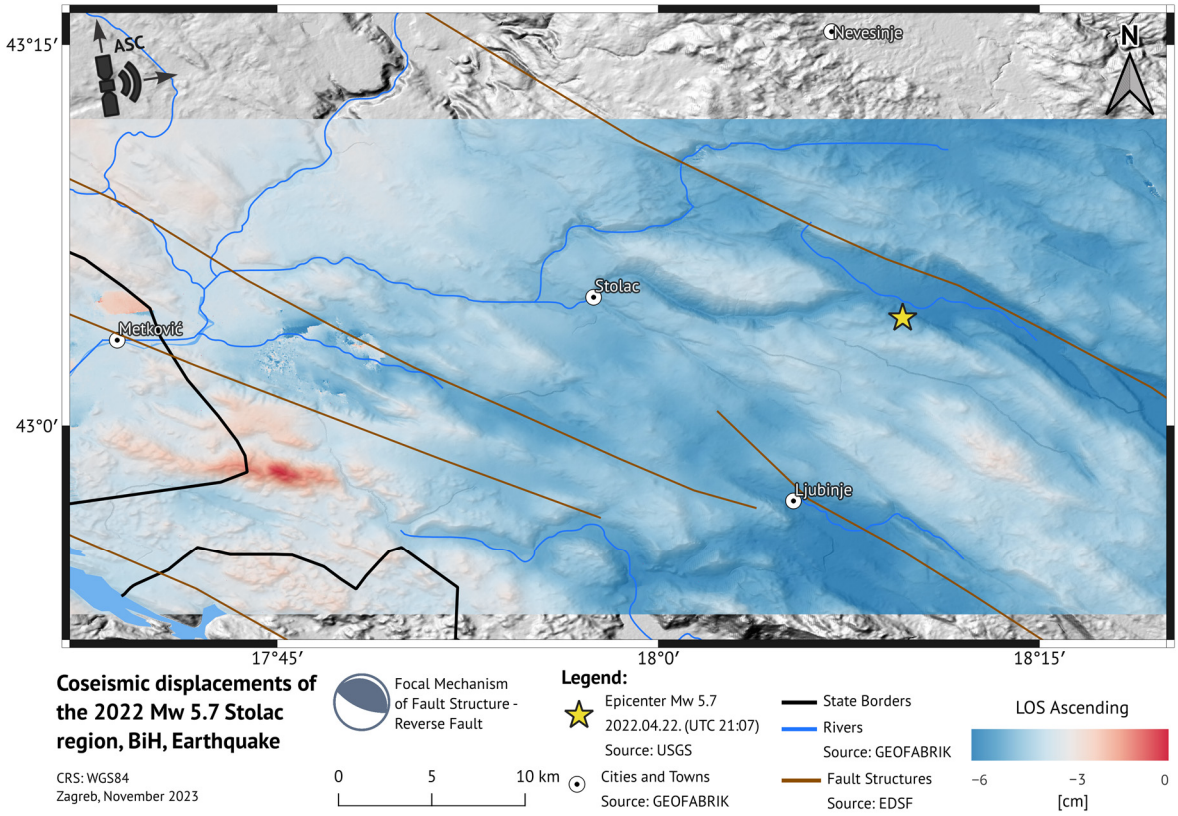


**Figure 11.** The LOS displacement map of the ascending orbit (track 73) of the coseismic deformation induced by the 2022 $M_w$ 5.7 Stolac earthquake.

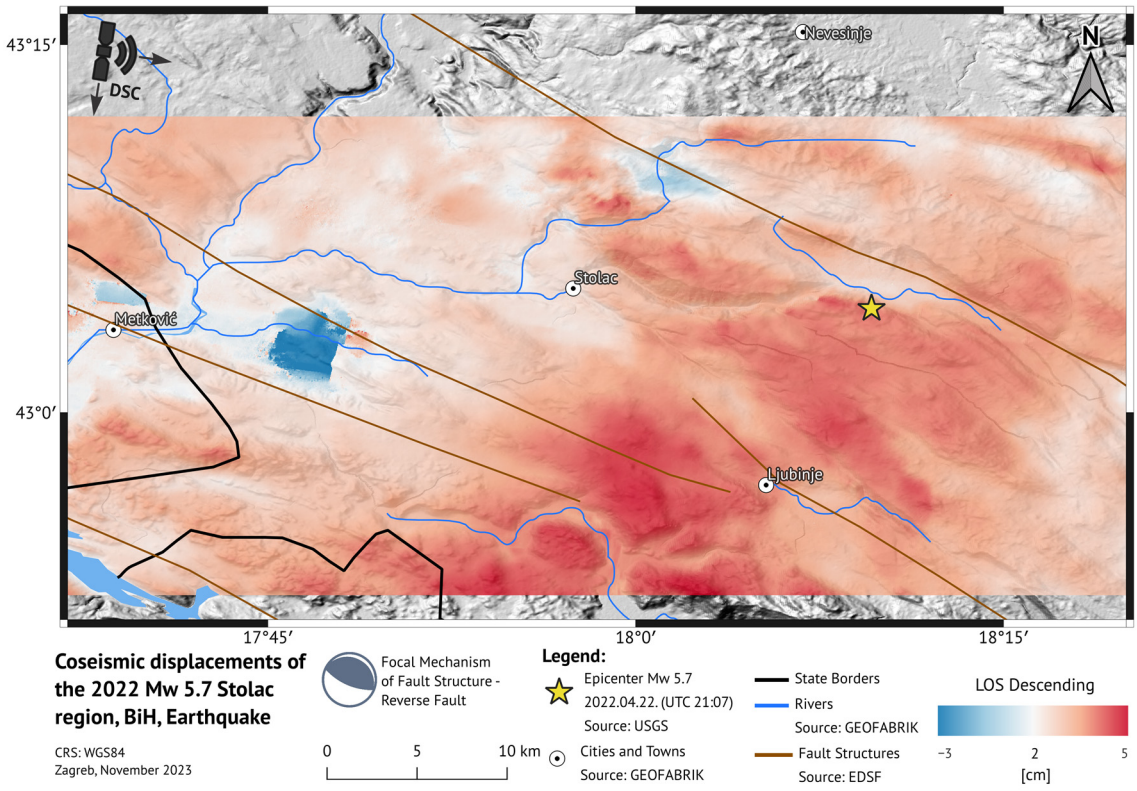


**Figure 12.** The LOS displacement map of the descending orbit (track 51) of the coseismic deformation induced by the 2022 $M_w$ 5.7 Stolac earthquake.

Displacements with values of opposite signs are depicted in Figures 11 and 12. The reason for this lies in the different observation geometries.

When the satellite orbits along an ascending almost polar orbit, it observes the Earth with a sensor oriented to the right, or eastward in terms of cardinal directions. However, when it observes in a descending orbit, following the "right-looking" convention, it will still sense the Earth's surface to the right, directing observations westward eastward in terms of cardinal directions. Different observation methods, among others, facilitate the correction of specific geometric errors in the images, like layover and foreshortening. Ultimately, this imaging approach enables the capture of 3D surface displacements of the Earth (Figure 13).

InSAR is limited to line-of-sight measurements of individual orbits and represents a one-dimensional displacement in the satellite's line-of-sight direction. Such spatial displacements consist of vertical displacement, horizontal displacement in the north–south direction and horizontal displacement in the east–west direction. The horizontal north–south displacement component is often neglected due to its low sensitivity of the measurements, which is a result of near-polar satellite orbits. With a combination of two independent acquisition modes (ascending and descending), horizontal and vertical displacements can be retrieved. Figure 13 and Equation (1) indicate a relationship between the acquisition geometry (the incidence angle ($\vartheta$) and azimuth angle ($\alpha$) of a satellite orbit) and LOS ascending and descending measurements [54]:

$$\begin{bmatrix} D_{HOR} \\ D_{VER} \end{bmatrix} = \begin{bmatrix} LOS_{ASC} \\ LOS_{DSC} \end{bmatrix} \cdot \begin{bmatrix} -cos\vartheta^{ASC} & cos\alpha^{ASC} sin\vartheta^{ASC} \\ -cos\vartheta^{DSC} & cos\alpha^{ASC} sin\vartheta^{DSC} \end{bmatrix} \quad (1)$$

where $D_{HOR}$ and $D_{VER}$ denote horizontal and vertical displacements.

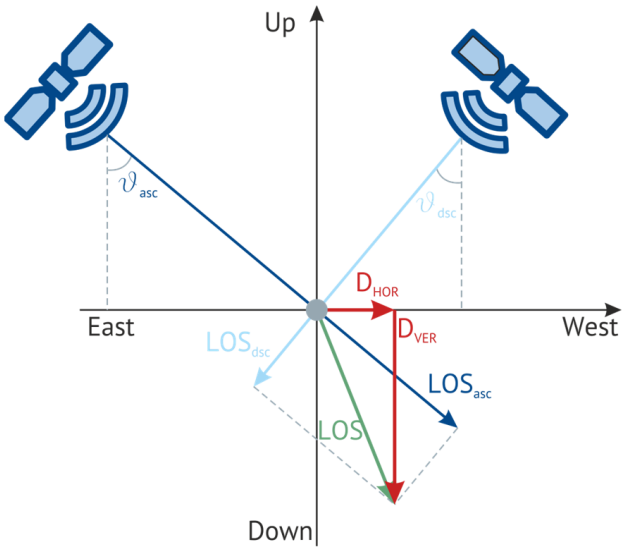


**Figure 13.** Decomposition of LOS displacements into vertical and horizontal E-W components using radar images acquired in ascending and descending geometry.

Figures 14 and 15 show preliminary derived coseismic horizontal east–west and vertical displacements after a 5.7 $M_w$ earthquake. Based on the preliminary data, it can be noticed that the observed area mostly moved horizontally to the east in the range of 5 cm to 8 cm. Some slight westward horizontal motion, in the range of 1 cm, or even no motion is detected in the southeast part of the research area. It can be concluded that the maximum horizontal motion is detected in the epicenter area, as well as around the city of Ljubinje, where a maximum eastward horizontal motion of 7 cm is detected. Horizontal displacements decrease as the distance from the epicenter increases.

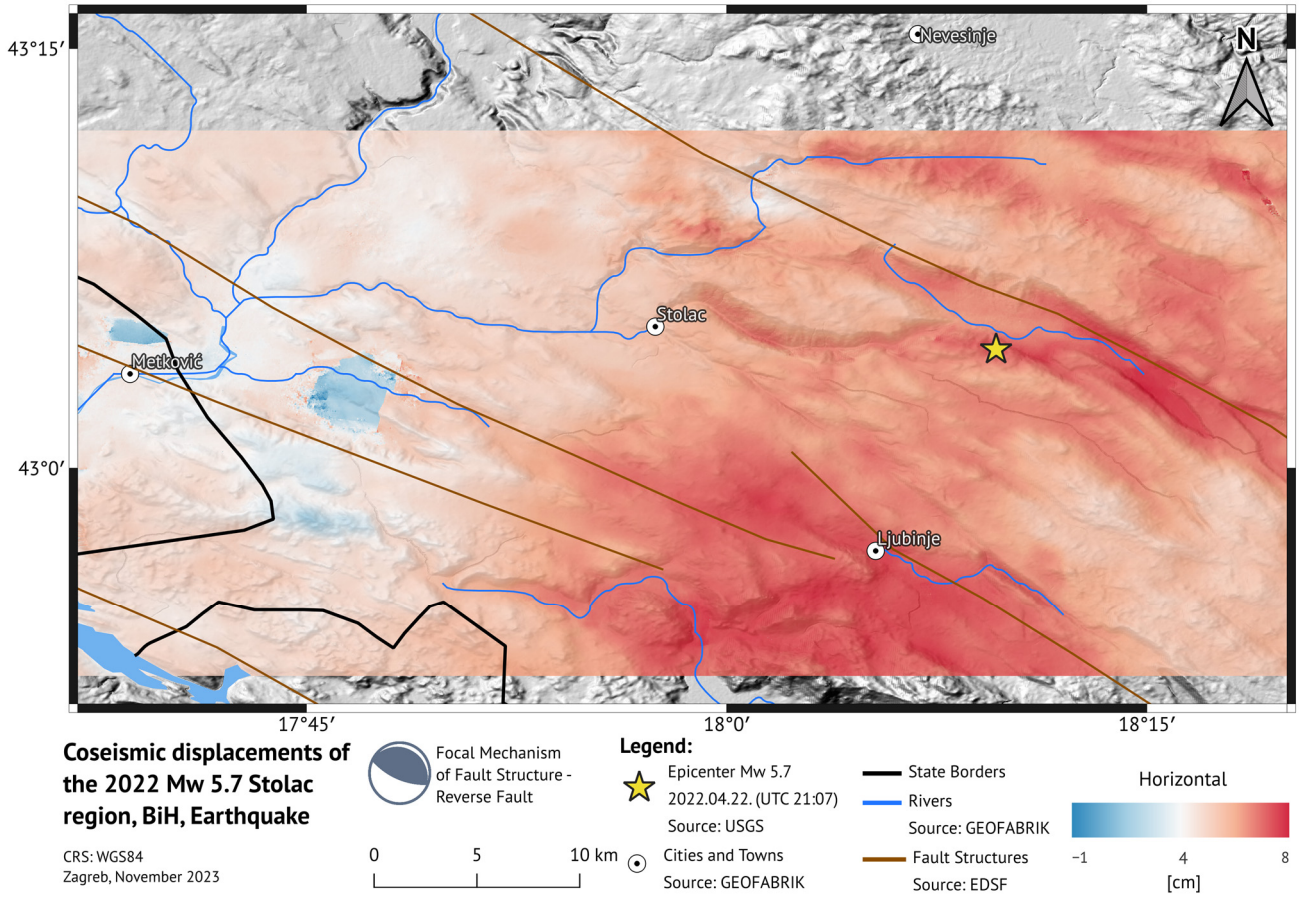


**Figure 14.** Derived preliminary coseismic horizontal motion in east–west direction.

It is possible that the westward motion in Figure 14, which is around 1 cm, is an outlier since this is an area around Svitavsko Lake, and hence these displacements should be interpreted with caution. Issues may have arisen during interferogram unwrapping if an appropriate mask was not applied.

On the other hand, vertical motion (Figure 15) has both the subsidence and uplift of the observed area. Most of the observed area has subsidence in the range of 1 cm to 2 cm. As in the horizontal motion, the area around the Svitavsko Lake should be interpreted with caution. The area surrounding the epicenter exhibits a 1 cm uplift in the southern part of the fault plane. Conversely, on the northern side of the fault plane and the epicenter, subsidence with a maximum value of around 2 cm has been detected.

As it is illustrated in Figure 15, aligning deep faults with DInSAR results validates the focal mechanism solution of the mainshock, portrayed in the form of a beachball diagram (Figure 15). Notably, the northern deep fault plane associated with the mainshock epicenter exhibits a subsidence pattern, whereas the southern fault plane demonstrates a slight uplift character. Furthermore, DInSAR findings indicate that the earthquake sequences did not induce any significant movements in fault mechanisms.

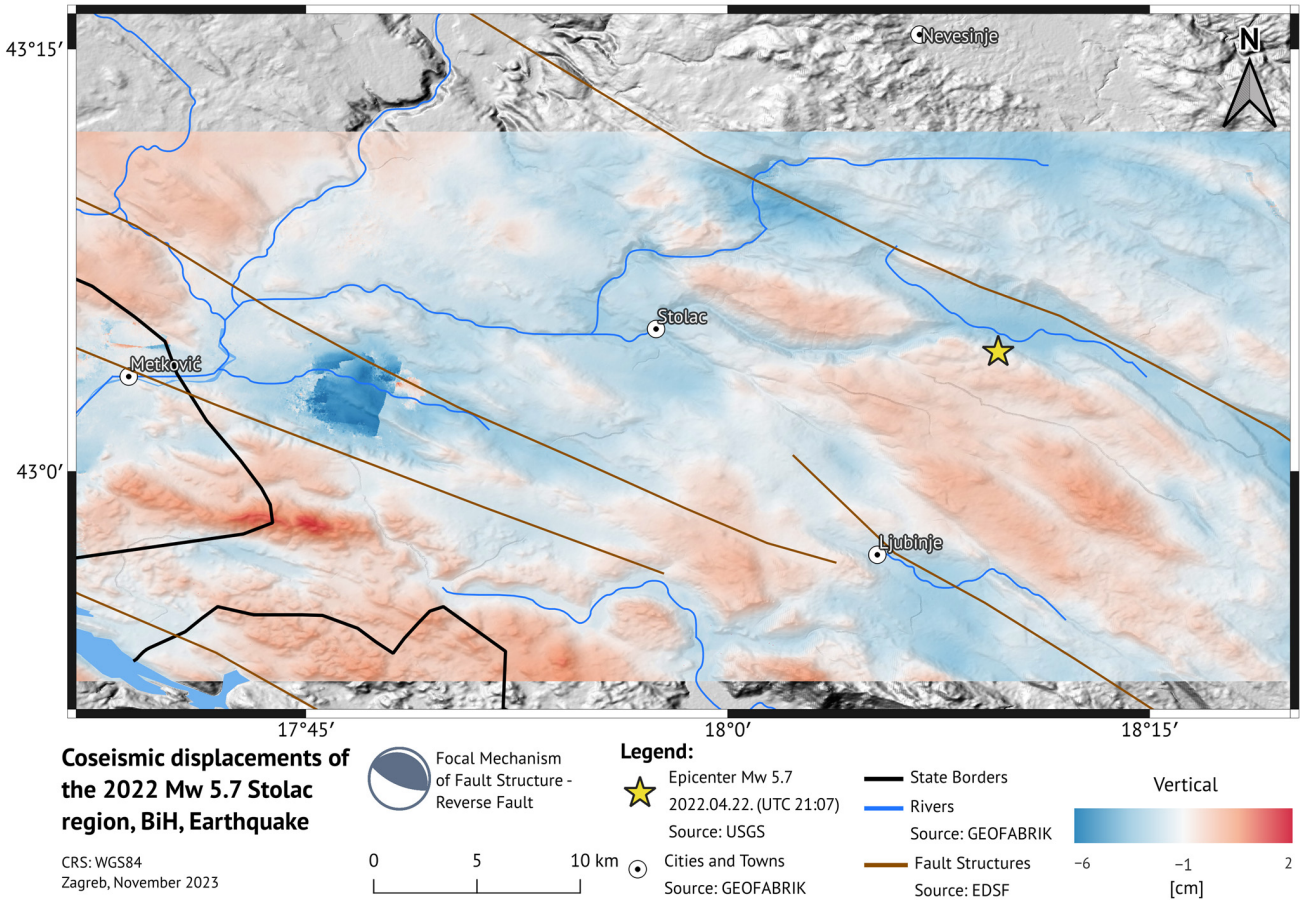


**Figure 15.** Derived preliminary coseismic vertical motion in sense of subsidence and uplift.

### *4.2. GNSS Processing*

GNSS data used in this study were collected within the Croatian Position System (CROPOS) at CORS Metković (MET3) located 41 km west from the mainshock's epicenter. We used a 5-day-long time series of a daily (24 h) GNSS position solution starting from 21 April and ending on 25 April 2022. Data were obtained with a Trimble Zephyr 3 geodetic antenna and Trimble Alloy receiver and were provided in RINEX format with a 1 s acquisition interval. Since the Trimble Zephyr 3 geodetic antenna supports both GPS and GLONASS positioning systems, the Canadian Spatial Reference System Precise Point Positioning Service (CSRS–PPP) [55] was used to process GNSS static solution data. Data were processed to ITRF2014 frame and were transformed to ETRF2000 using the ETRF/ITRF Coordinate transformation Tool [56]. In the end, data were converted to the plane of HTRS96/TM projection (EPSG:3765). The mean daily coordinate values, as well as the reference data obtained after the CROPOS network adjustment, which represent the MET3 station coordinates, are presented in Table 3.

**Table 3.** The MET3 HTRS96/TM coordinates include reference data for July 2021 obtained after CROPOS network adjustment, while the data for April 2022 pertain to earthquake observations a few days before and after the earthquake.

| Date | E [m] | N [m] | h [m] | Epoch |
|---|---|---|---|---|
| 1 July 2021 | 593,674.5002 | 4,769,130.4565 | 60.186 | 2021.50 |
| 21 April 2022 | 593,674.4995 | 4,769,130.4636 | 60.180 | 2022.30 |
| 22 April 2022 | 593,674.5025 | 4,769,130.4635 | 60.181 | 2022.31 |
| 23 April 2022 | 593,674.5000 | 4,769,130.4628 | 60.185 | 2022.31 |
| 24 April 2022 | 593,674.4997 | 4,769,130.4666 | 60.178 | 2022.31 |
| 25 April 2022 | 593,674.5006 | 4,769,130.4636 | 60.181 | 2022.32 |

In Table 4, the standard deviations of the coordinates obtained by the CSRS-PPP method processing GNSS measurements at station MET3 are presented. Standard deviations are expressed within a 2σ confidence level. The easting and northing components of the coordinates deviate within 2 mm, while the vertical coordinate approaches a level of nearly 1 cm.

**Table 4.** The standard deviations of the coordinates derived from CSRS–PPP within a 2σ confidence level.

| Date | $\sigma_E$ [mm] | $\sigma_N$ [mm] | $\sigma_h$ [mm] | Epoch |
|---|---|---|---|---|
| 21 April 2022 | 2 | 2 | 8 | 2022.30 |
| 22 April 2022 | 2 | 2 | 7 | 2022.31 |
| 23 April 2022 | 2 | 2 | 8 | 2022.31 |
| 24 April 2022 | 2 | 2 | 8 | 2022.31 |
| 25 April 2022 | 2 | 2 | 7 | 2022.32 |

Figure 16 shows the mean daily displacements of MET3 station coordinates in reference to three axes (east–west, north–south and up–down) in the days just before and after the earthquake's mainshock. It is worth noting that no significant displacements at the MET3 station were detected by the PPP method. The largest displacements were observed on 24 April, the day of the last recorded aftershock, where subsidence in the range of 7 mm and 10 mm horizontal north–south displacements were observed. From Figure 15, it can be deducted that no major displacements happened at the MET3 station at the time of the earthquake.

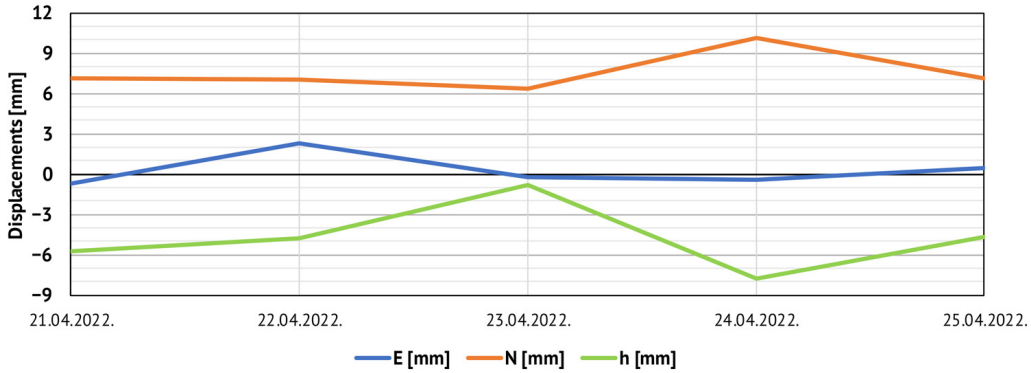


**Figure 16.** Mean daily coordinate displacements of MET3 station in days just before and after earthquake's mainshock. Coordinates displacements were determined in relation to reference data.

## 5. Discussion

DInSAR-derived displacements at the MET3 station and its vicinity can be observed in Figure 17. According to DInSAR, derived coseismic displacements, a 1 cm subsidence and 4 cm eastward horizontal motion can be observed.

DInSAR coseismic displacements were compared to independent GNSS data sources. To determine the displacement immediately before, during and after the earthquake's mainshock, it is inevitable to determine the coordinates for each individual measurement epoch. The data for vertical and horizontal motion were calculated with the use of the kinematic processing of the CSRS-PPP service and were transformed into HTRS96/TM projection using the abovementioned steps. The displacements were determined by subtracting the mean daily value determined by PPP and the data for each second. In Figure 18, vertical motion is expressed. The vertical motion varies between 6.4 cm and 2.1 cm which corresponds to subsidence and uplift, respectively. Following Figure 18, large-scale oscillation can be observed with an arithmetic mean of −1.4 cm with the associated standard deviation of ±1.5 cm.

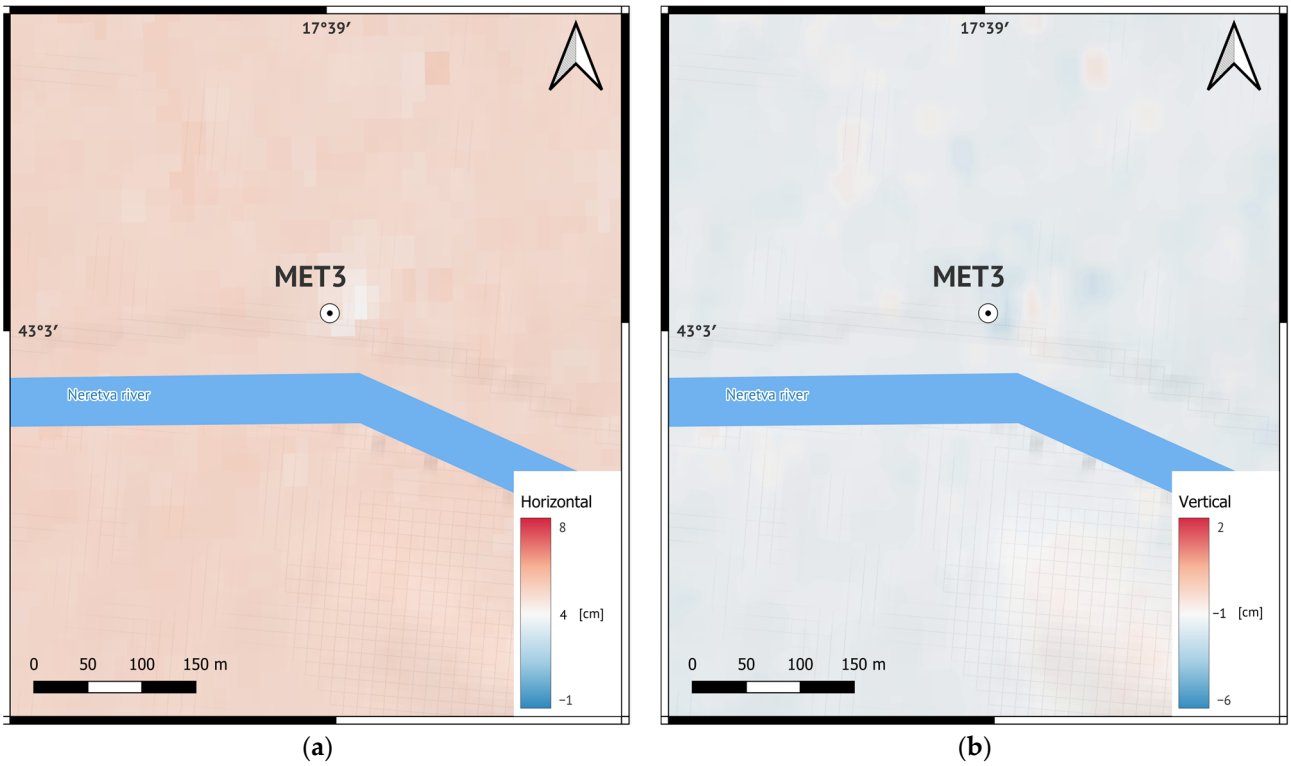


**Figure 17.** DInSAR-derived displacements at the MET3 station, where (**a**) shows horizontal displacements, and (**b**) shows vertical displacements.

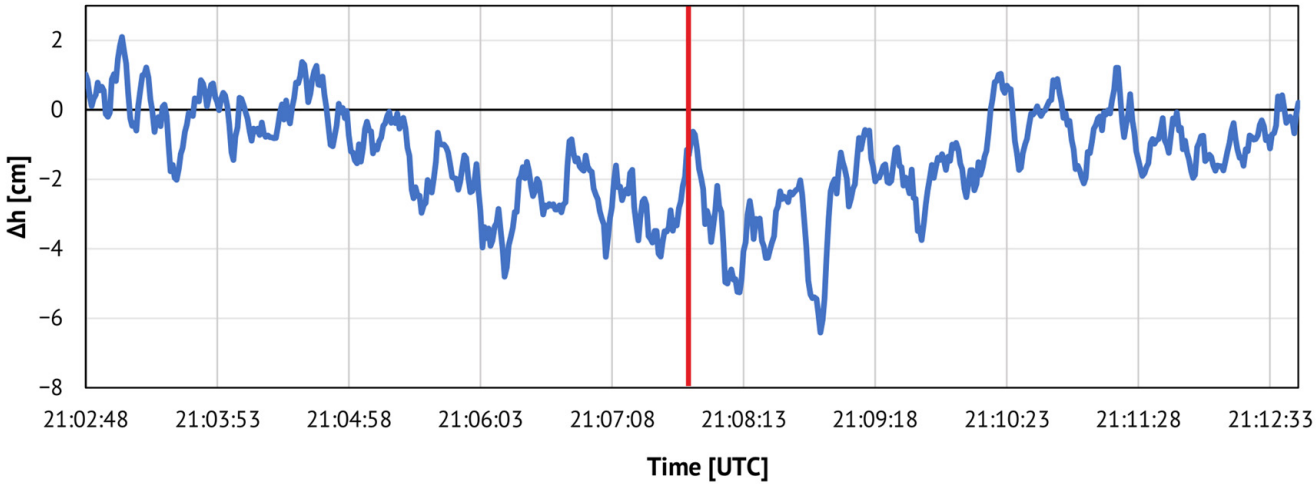


**Figure 18.** A graph which shows subsidence and uplift in the span of 5 min before and after the earthquake's mainshock (21:07:48 UTC), where the mainshock in the graph is represented with a red line. The red vertical line represents the time of the earthquake mainshock.

On the other hand, horizontal displacements have no significant oscillations. The minimum value corresponds to 1.9 cm westward horizontal motion, while 2.1 cm eastward horizontal motion is detected (Figure 19). The arithmetic mean for the 10 min time span is 0.3 cm with an associated standard deviation of ±0.6 cm.

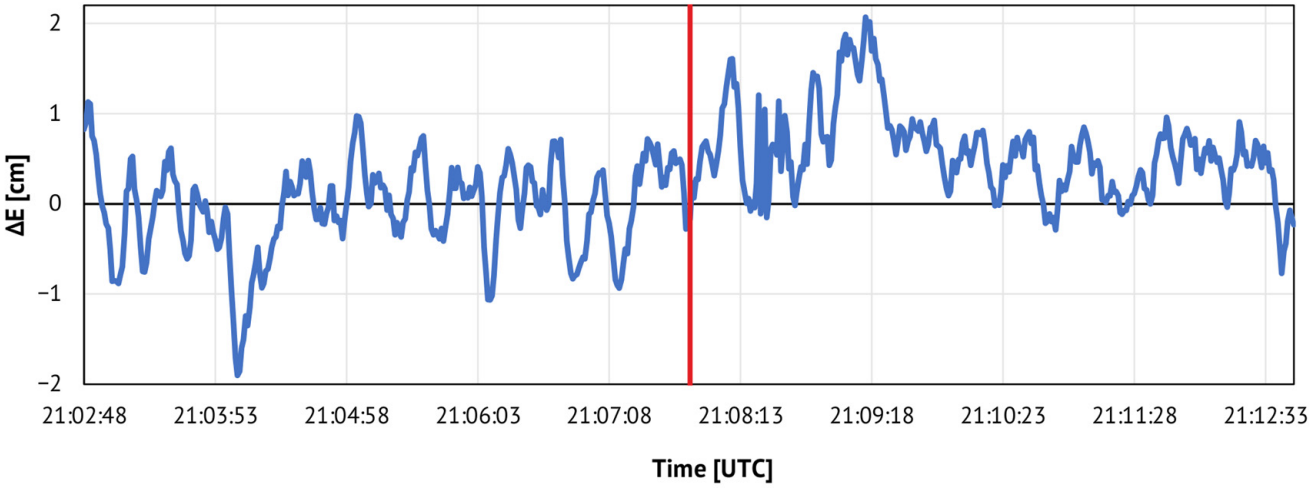


**Figure 19.** A graph which shows E-W horizontal motion in the span of 5 min before and after the earthquake's mainshock (21:07:48 UTC), where the mainshock in the graph is represented with a red line.

As mentioned before, DInSAR analysis has validated trends in the structural configuration of the region's fault systems, demonstrating that the epicenter of the mainshock activated a reverse fault (Figure 15). As depicted in Figure 4, reverse faults predominate in the research area, which constitutes a segment of the External Dinarides. Nonetheless, there are occasional outliers in the form of normal and strike-slip faulting systems, albeit in small variations, as indicated in Figure 1. It is noteworthy that the aftershocks observed in this region exhibit characteristics of normal faulting geometries.

## 6. Conclusions

We determined the coseismic displacements of the $M_w$ 5.7 Stolac earthquake using two differential interferograms from the Sentinel-1 satellite mission. The results were later tried to be confirmed with the GNSS time series data at the GNSS (CROPOS) station MET3. Static and kinematic data solutions at the MET3 station did not entirely confirm DInSAR results, and a reason can be due to the relatively long distance from the earthquake's epicenter. Another problem with confirming DInSAR displacements was that the data from the nearest GNSS (Republic of Srpska Positioning System—SRPOS) station NEVE were not available, while the GNSS (Federation of Bosnia and Hercegovina Positioning System—FBiHPOS) station MOST did not have sufficiently high-quality data for comparison. Another problem that can influence DInSAR results concerns topography, especially coherence. Coherence over the studied area had satisfactory values but was not ideal because the studied area is mostly hilly area with a lot of vegetation.

For future research, it is proposed to use data from the newly established GNSS station of the Pelješac Bridge monitoring system to compare results. Additionally, it would be ideal to expand the research area for comparison with at least one more continuously operational reference station. Furthermore, the application of Sentinel-2 data for vegetation filtering is suggested to improve coherence assessment and image quality. Also, an L-band operating radar system can be used to better penetrate through low vegetation which covers large parts of the study area.

It is essential to emphasize that, for a comprehensive analysis, determining the north–south shift is necessary.

This research confirms that connecting geodetic observations, such as InSAR, with present geological structures can provide valuable insights into the dynamics of the Earth's crust and seismic activity. By integrating geodetic data with existing geological knowledge, a more comprehensive understanding of the region's tectonic setting, fault systems and seismic hazards can be offered.

**Author Contributions:** General idea, M.P.; conceptualization, M.P. and F.M.; methodology, M.P. and F.M.; software, A.B.; validation, M.P. and T.B.; formal analysis, F.M. and A.B.; investigation, F.M. and A.B.; resources, F.M. and A.B.; data curation, A.B.; writing—original draft preparation, F.M.; writing—review and editing, A.B.; visualization, A.B. and F.M.; supervision, M.P.; project administration, M.P.; funding acquisition, M.P. All authors have read and agreed to the published version of the manuscript.

**Funding:** This research received no external funding.

**Data Availability Statement:** Sentinel-1 SAR images are available through the Alaska Satellite Facility Vertex website (ASF; https://search.asf.alaska.edu/#/, accessed on 10 January 2024); topographic phase delay maps are available through the Generic Atmospheric Correction Online Service website (GACOS; http://www.gacos.net/, accessed on 10 January 2024); focal mechanism solutions are available at U.S. Geological Survey (USGS; https://earthquake.usgs.gov/earthquakes/search/, accessed on 15 January 2024), European–Mediterranean Regional Centroid-Moment Tensors (RCMT; http://rcmt2.bo.ingv.it, accessed on 15 January 2024); earthquake catalogues are available at the Earthquake Hazard and Risk across Europe (http://www.efehr.org/start/, accessed on 14 January 2024), International Seismological Centre Global Instrumental Earthquake Catalogue (ISC-GEM; https://doi.org/10.31905/d808b825, accessed on 14 January 2024) and U.S. Geological Survey (USGS; https://earthquake.usgs.gov/earthquakes/search/, accessed on 10 January 2024) website; world stress map data are available at the (WSM; https://www.world-stress-map.org/, accessed on 16 January 2024) website; fault data are available at the European Database of Seismogenic Faults website (EDSF; https://edsf13.ingv.it/index.html, accessed on 16 January 2024); rivers, urban areas and administrative borders are available at GEOFABRIK (https://www.geofabrik.de/, accessed on 13 February 2024) and GNSS time series data are not public.

**Acknowledgments:** The authors want to thank Snježana Markušić, for giving permission to use Figure 4 from reference [42].

**Conflicts of Interest:** The authors declare no conflicts of interest.

## References

1. USGS. United States Geological Survey Earthquake Hazards Program. Available online: https://www.usgs.gov/programs/earthquake-hazards/earthquakes (accessed on 10 January 2024).
2. RCMT. European-Mediterranean Regional Centroid-Moment Tensors. Available online: http://rcmt2.bo.ingv.it (accessed on 9 January 2024).
3. Ademović, N.; Kalman Šipoš, T.; Hadzima-Nyarko, M. Rapid assessment of earthquake risk for Bosnia and Herzegovina. *Bull. Earthq. Eng.* **2020**, *18*, 1835–1863. [CrossRef]
4. Markušić, S.; Herak, M. Seismic Zoning of Croatia. *Nat. Hazards* **1998**, *18*, 269–285. [CrossRef]
5. Omerbashich, M.; Sijarić, G. Seismotectonics of Bosnia—Overview. *Acta Geodyn. Geomater.* **2006**, *3*, 17–29.
6. Milev, G.; Vassileva, K. Geodynamics of the Balkan Peninsula and Bulgaria. In Proceedings of the International Symposium on Strong Vrancea Earthquakes and Risk Mitigation, Bucharest, Romania, 4–6 October 2007.
7. Oldow, J.S.; Ferranti, L.; Lewis, D.S.; Campbell, J.K.; D'Argenio, B.; Catalano, R.; Pappone, G.; Carmignani, L.; Conti, P.; Aiken, C.L.V. Active fragmentation of Adria, the north African promontory, central Mediterranean orogen. *Geology* **2002**, *30*, 779–782. [CrossRef]
8. Tari, V. Evolution of the northern and western Dinarides: A tectonostratigraphic approach. *Stephan Mueller Spec. Publ. Ser.* **2002**, *1*, 223–236. [CrossRef]
9. Balling, P.; Tomljenović, B.; Schmid, S.M.; Ustaszewski, K. Contrasting along-strike deformation styles in the central external Dinarides assessed by balanced cross-sections: Implications for the tectonic evolution of its Paleogene flexural foreland basin system. *Glob. Planet. Change* **2021**, *205*, 103587. [CrossRef]
10. Ademović, N.; Demir, V.; Cvijić-Amulić, S.; Málek, J.; Prachař, I.; Vackář, J. Compilation of the seismic hazard maps in Bosnia and Herzegovina. *Soil Dyn. Earthq. Eng.* **2021**, *141*, 106500. [CrossRef]
11. Hrvatović, H. *Identifikacija i Procjena Geoloških Hazarda-Zemljotresa*; Ministry of Security of Bosnia and Herzegovina: Sarajevo, Bosnia and Herzegovina, 2010.
12. Hrvatović, H. *Geological Guidebook through Bosnia and Herzegovina*; Geological Survey: Sarajevo, Bosnia and Herzegovina, 2005; pp. 1–163.
13. Hrvatović, H. *Geological Map of Bosnia and Herzegovina*; Geological Survey: Sarajevo, Bosnia and Herzegovina, 2009.
14. Grünthal, G.; Wahlström, R. The European-Mediterranean Earthquake Catalogue (EMEC) for the last millennium. *J. Seismol.* **2012**, *16*, 535–570. [CrossRef]
15. Rovida, A.; Antonucci, A. *EPICA—European PreInstrumental Earthquake Catalogue*; Version 1.1, Dataset; Istituto Nazionale di Geofisica e Vulcanologia (INGV): Rome, Italy, 2021. [CrossRef]

16. Danciu, L.; Nandan, S.; Reyes, C.; Basili, R.; Weatherill, G.; Beauval, C.; Rovida, A.; Vilanova, S.; Sesetyan, K.; Bard, P.-Y.; et al. *The 2020 Update of the European Seismic Hazard Model: Model Overview*; EFEHR Technical Report 001, v1.0.0; 2021. Available online: https://gitlab.seismo.ethz.ch/efehr/eshm20/-/blob/master/documentation/EFEHR_TR001_ESHM20.pdf (accessed on 15 January 2024). [CrossRef]
17. Massonnet, D.; Rossi, M.; Carmona, C.; Adragna, F.; Peltzer, G.; Feigl, K.; Rabaute, T. The displacement field of the Landers earthquake mapped by radar interferometry. *Nature* **1993**, *364*, 138–142. [CrossRef]
18. Wang, G.; Xie, M.; Chai, X.; Wang, L.; Dong, C. D-InSAR-based landslide location and monitoring at Wudongde hydropower reservoir in China. *Environ. Earth. Sci.* **2013**, *69*, 2763–2777. [CrossRef]
19. Manzo, M.; Ricciardi, G.P.; Casu, F.; Ventura, G.; Zeni, G.; Borgström, S.; Lanari, R. Surface deformation analysis in the Ischia Island (Italy) based on spaceborne radar interferometry. *J. Volcanol. Geotherm. Res.* **2006**, *151*, 399–416. [CrossRef]
20. Tzouvaras, M.; Danezis, C.; Hadjimitsis, D.G. Differential SAR Interferometry Using Sentinel-1 Imagery-Limitations in Monitoring Fast Moving Landslides: The Case Study of Cyprus. *Geosciences* **2020**, *10*, 236. [CrossRef]
21. Mulić, M.; Bašagić, M.; Čičić, S. Geodynamic Investigation in Bosnia and Herzegovina. In *The Adria Microplate: GPS Geodesy, Tectonics and Hazards*; Nato Science Series: IV: Earth and Environmental Sciences; Pinter, N., Gyula, G., Weber, J., Stein, S., Medak, D., Eds.; Kluwer Academic Publishers: Dordrecht, The Netherlands, 2006; Volume 61, pp. 195–207. [CrossRef]
22. Čičić, S.; Bašagić, M. Geological map of Bosnia and Herzegovina 1: 300.000: Content and application. *Rep. Geod.* **2006**, *5*, 93–110.
23. Schmid, S.M.; Fügenschuh, B.; Kounov, A.; Maţenco, L.; Nievergelt, P.; Oberhänsli, R.; Pleuger, J.; Schefer, S.; Schuster, R.; Tomljenović, B.; et al. Tectonic units of the Alpine collision zone between Eastern Alps and western Turkey. *Gondwana Res.* **2019**, *78*, 308–374. [CrossRef]
24. Smailbegović, A.; Korajlić, N.; Toth, I. Overall Seismic Risk in Bosnia-Herzegovina/Dalmatia Region of Croatia and Elements of Perfect Crisis in an Earthquake Aftermath. *Ann. Disaster Risk Sci.* **2020**, *3*, 1–9. [CrossRef]
25. Balling, P.; Tomljenović, B.; Herak, M.; Ustaszewski, K. Impact of mechanical stratigraphy on deformation style and distribution of seismicity in the central External Dinarides: A 2D forward kinematic modelling study. *Swiss J. Geosci.* **2023**, *116*, 7. [CrossRef]
26. Anderson, H.; Jackson, J. Active Tectonics of the Adriatic Region. *Geophys. J. Int.* **1987**, *91*, 937–983. [CrossRef]
27. Marjanović, M. *Application of GPS Measurements for Determining Horizontal and Vertical Movements of the Adriatic Microplate*; Faculty of Geodesy, University of Zagreb: Zagreb, Croatia, 2008.
28. Pavasović, M. *CROPOS kao Hrvatski Terestrički Referentni Okvir i Njegova Primjena u Geodinamičkim Istraživanjima (CROPOS as Croatian Terrestrial Reference Frame and Its Application in Geodynamic Researches)*; Faculty of Geodesy, University of Zagreb: Zagreb, Croatia, 2014.
29. Pavasović, M.; Đapo, A.; Marjanović, M.; Pribičević, B. Present Tectonic Dynamics of the Geological Structural Setting of the Eastern Part of the Adriatic Region Obtained from Geodetic and Geological Data. *Appl. Sci.* **2021**, *11*, 5735. [CrossRef]
30. Heidbach, O.; Rajabi, M.; Reiter, K.; Ziegler, M. *World Stress Map Database Release 2016*; Services, G.D., Ed.; GFZ German Research Centre for Geosciences: Potsdam, Germany, 2016.
31. Šumanovac, F.; Orešković, J.; Grad, M.; ALP 2002 Working Group. Crustal structure at the contact of the Dinarides and Pannonian basin based on 2-D seismic and gravity interpretation of the Alp07 profile in the ALP 2002 experiment. *Geophys. J. Int.* **2009**, *179*, 615–633. [CrossRef]
32. Korbar, T. Orogenic evolution of the External Dinarides in the NE Adriatic region: A model constrained by tectonostratigraphy of Upper Cretaceous to Paleogene carbonates. *Earth-Sci. Rev.* **2009**, *96*, 296–312. [CrossRef]
33. Lombardi, D.; Braunmiller, J.; Kissling, E.; Giardini, D. Moho depth and Poisson's ratio in the Western-Central Alps from receiver functions. *Geophys. J. Int.* **2008**, *173*, 249–264. [CrossRef]
34. Caporali, A.; Aichhornm, C.; Barlik, M.; Becker, M.; Fejes, I.; Gerhatova, L.; Ghitau, D.; Grenerczy, G.; Hefty, J.; Krauss, S.; et al. Surface kinematics in the Alpine–Carpathian–Dinaric and Balkan region inferred from a new multi-network GPS combination solution. *Tectonophysics* **2009**, *474*, 295–321. [CrossRef]
35. Stipčević, J.; Herak, M.; Molinari, I.; Dasović, I.; Tkalčić, H.; Gosar, A. Crustal thickness beneath the Dinarides and surrounding areas from receiver functions. *Tectonics* **2020**, *39*, e2019TC005872. [CrossRef]
36. Zailac, K.; Matoš, B.; Vlahović, I.; Stipčević, J. Reference seismic crustal model of the Dinarides. *Solid Earth* **2023**, *14*, 1197–1220. [CrossRef]
37. Cavazza, W.; Roure, F.; Ziegler, P.A. The Mediterranean Area and the Surrounding Regions: Active Processes, Remnants of Former Tethyan Oceans and Related Thrust Belts. In *The TRANSMED Atlas. The Mediterranean Region from Crust to Mantle*, 1st ed.; Cavazza, W., Roure, F., Spakman, W., Stampfli, G.M., Ziegler, P.A., Eds.; Springer: Berlin/Heidelberg, Germany, 2004; pp. 1–29. [CrossRef]
38. Lee, V.; Herak, M.; Herak, D.; Trifunac, M. Uniform hazard spectra in western Balkan Peninsula. *Soil Dyn. Earthq. Eng.* **2013**, *55*, 1–20. [CrossRef]
39. Giardini, D.; Basham, P. The Global Seismic Hazard Assessment Program (GSHAP). *Ann. Geophys.* **1993**, *36*, 3–13. [CrossRef]
40. Giardini, D.; Grünthal, G.; Shedlock, K.M.; Zhang, P. The GSHAP Global Seismic Hazard Model. *Ann. Geophys.* **1999**, *42*, 1225–1230. [CrossRef]
41. Slejko, D.; Camassi, R.; Cecić, I.; Herak, D.; Herak, M.; Kociu, S.; Kouskouna, V.; Lapajne, J.; Makropoulos, K.; Meletti, C. Seismic hazard assessment for Adria. *Ann. Geophys.* **1999**, *42*, 1085–1107. [CrossRef]

42. Markušić, S.; Gülerce, Z.; Kuka, N.; Duni, L.; Ivančić, I.; Radovanović, S.; Glavatović, B.; Milutinović, Z.; Akkar, S.; Kovačević, S.; et al. An updated and unified earthquake catalogue for the Western Balkan Region. *Bull. Earthq. Eng.* **2016**, *14*, 321–343. [CrossRef]
43. Mihaljević, J.; Zupančič, P.; Kuka, N.; Kaluđerović, N.; Koçi, R.; Markušić, S.; Šalić, R.; Dushi, E.; Begu, E.; Duni, L.; et al. BSHAP seismic source characterization models for the Western Balkan region. *Bull. Earthq. Eng.* **2017**, *15*, 3963–3985. [CrossRef]
44. ISC-GEM. International Seismological Centre Global Instrumental Earthquake Catalogue. 2023. Available online: http://www.isc.ac.uk/iscgem/download.php (accessed on 10 January 2024). [CrossRef]
45. Bijedić, A. *Pregled Zemljotresa na Području Bosne i Hercegovine*; Federal Hydrometeorological Institute: Sarajevo, Bosnia and Herzegovina, 2014.
46. European Space Agency (ESA). Available online: https://sentiwiki.copernicus.eu/ (accessed on 2 February 2024).
47. Rosen, P.A.; Gurrola, E.M.; Agram, P.; Cohen, J.; Lavalle, M.; Riel, B.V.; Fattahi, H.; Aivazis, M.A.; Simons, M.; Buckley, S.M. The InSAR scientific computing environment 3.0: A flexible framework for NISAR operational and user-led science processing. In Proceedings of the IGARSS 2018—2018 IEEE International Geoscience and Remote Sensing Symposium, Valencia, Spain, 22–27 July 2018; pp. 4897–4900. [CrossRef]
48. Farr, T.G.; Rosen, P.A.; Caro, E.; Crippen, R.; Duren, R.; Hensley, S.; Kobrick, M.; Paller, M.; Rodriguez, E.; Roth, L.; et al. The Shuttle Radar Topography Mission. *Rev. Geophys.* **2007**, *45*, RG2004. [CrossRef]
49. Goldstein, R.M.; Werner, C.L. Radar interferogram filtering for geophysical applications. *Geophys. Res. Lett.* **1998**, *25*, 4035–4038. [CrossRef]
50. Chen, C.W.; Zebker, H.A. Two-dimensional phase unwrapping with use of statistical models for cost functions in nonlinear optimization. *J. Opt. Soc. Am.* **2001**, *18*, 338–351. [CrossRef] [PubMed]
51. Yu, C.; Penna, N.T.; Li, Z. Generation of real-time mode high-resolution water vapor fields from GPS observations. *J. Geophys. Res. Atmos.* **2017**, *122*, 2008–2025. [CrossRef]
52. Yu, C.; Li, Z.; Penna, N.T. Interferometric synthetic aperture radar atmospheric correction using a GPS-based iterative tropospheric decomposition model. *Remote Sens. Environ.* **2018**, *204*, 109–121. [CrossRef]
53. Yu, C.; Li, Z.; Penna, N.T.; Crippa, P. Generic atmospheric correction model for interferometric synthetic aperture radar observations. *J. Geophys. Res. Solid Earth* **2018**, *123*, 9202–9222. [CrossRef]
54. Mora, O.; Ordoqui, P.; Iglesias, R.; Blanco, P. Earthquake Rapid Mapping Using Ascending and Descending Sentinel-1 TOPSAR Interferograms. *Procedia Comput. Sci.* **2016**, *100*, 1135–1140. [CrossRef]
55. CSRS-PPP. Canadian Spatial Reference System Precise Point Positioning Service. Available online: https://webapp.csrs-scrs.nrcan-rncan.gc.ca/geod/tools-outils/ppp.php (accessed on 21 October 2022).
56. ECTT. ETRF/ITRF Coordinate Transformation Tool. Available online: https://www.epncb.oma.be/_productsservices/coord_trans/ (accessed on 22 October 2022).